


Wintertime Synoptic Patterns of Midlatitude Boundary Layer Clouds Over the Western North Atlantic: Climatology and Insights From In Situ ACTIVATE Observations

David Painemal^{1,2} , Seethala Chellappan³ , William L. Smith Jr.², Douglas Spangenberg^{1,2}, J. Minnie Park⁴ , Andrew Ackerman⁵ , Jingyi Chen⁶ , Ewan Crosbie^{1,2} , Richard Ferrare² , Johnathan Hair² , Simon Kirschler^{7,8} , Xiang-Yu Li⁶, Allison McComiskey⁴ , Richard H. Moore² , Kevin Sanchez² , Armin Sorooshian^{9,10}, Florian Tornow^{5,11} , Christiane Voigt^{7,8} , Hailong Wang⁶ , Edward Winstead^{1,2} , Xubin Zeng¹⁰, Luke Ziemba² , and Paquita Zuidema³ 

¹Science Systems and Applications, Inc, Hampton, VA, USA, ²NASA Langley Research Center, Hampton, VA, USA, ³Rosenstiel School of Marine and Atmospheric, and Earth Sciences, University of Miami, Miami, FL, USA, ⁴Brookhaven National Laboratory, Upton, NY, USA, ⁵NASA Goddard Institute for Space Sciences, New York, NY, USA, ⁶Pacific Northwest National Laboratory, Richland, WA, USA, ⁷Institut für Physik der Atmosphäre, Deutsches Zentrum für Luft- und Raumfahrt (DLR), Oberpfaffenhofen, Germany, ⁸Institut für Physik der Atmosphäre, Johannes Gutenberg-Universität, Mainz, Germany, ⁹Department of Chemical and Environmental Engineering, University of Arizona, Tucson, AZ, USA, ¹⁰Department of Hydrology and Atmospheric Sciences, University of Arizona, Tucson, AZ, USA, ¹¹Columbia University, New York City, NY, USA

Key Points:

- Winter synoptic evolution is well described by a clustering method applied to 600 hPa geopotential height
- Marine low clouds are characteristic of the trough regime, associated with strong surface heat fluxes
- Cold-air outbreaks are associated with trough and ridge–trough regimes, and witness peaks in cloud droplet number and aerosol concentrations

Supporting Information:

Supporting Information may be found in the online version of this article.

Correspondence to:

D. Painemal,
david.painemal@nasa.gov

Citation:

Painemal, D., Chellappan, S., Smith, W. L. Jr., Spangenberg, D., Park, J. M., Ackerman, A., et al. (2023). Wintertime synoptic patterns of midlatitude boundary layer clouds over the western North Atlantic: Climatology and insights from in situ ACTIVATE observations. *Journal of Geophysical Research: Atmospheres*, 128, e2022JD037725. <https://doi.org/10.1029/2022JD037725>

Received 25 AUG 2022
Accepted 26 MAR 2023

Abstract The winter synoptic evolution of the western North Atlantic and its influence on the atmospheric boundary layer is described by means of a regime classification based on Self-Organizing Maps applied to 12 years of data (2009–2020). The regimes are classified into categories according to daily 600-hPa geopotential height: dominant ridge, trough to ridge eastward transition (trough–ridge), dominant trough, and ridge to trough eastward transition (ridge–trough). A fifth synoptic regime resembles the winter climatological mean. Coherent changes in sea-level pressure and large-scale winds are in concert with the synoptic regimes: (a) the ridge regime is associated with a well-developed anticyclone; (b) the trough–ridge gives rise to a low-pressure center over the ocean, ascents, and northerly winds over the coastal zone; (c) trough is associated with the eastward displacement of a cyclone, coastal subsidence, and northerly winds, all representative characteristics of cold-air outbreaks; and (d) the ridge–trough regime features the development of an anticyclone and weak coastal winds. Low clouds are characteristic of the trough regime, with both trough and trough–ridge featuring synoptic maxima in cloud droplet number concentration (N_d). The N_d increase is primarily observed near the coast, concomitant with strong surface heat fluxes exceeding by more than 400 W m^{-2} compared to fluxes further east. Five consecutive days of aircraft observations collected during the ACTIVATE campaign corroborates the climatological characterization, confirming the occurrence of high N_d for days identified as trough. This study emphasizes the role of boundary-layer dynamics and aerosol activation and their roles in modulating cloud microphysics.

Plain Language Summary The synoptic evolution of boundary layer clouds over the western North Atlantic is described by means of a regime classification based on Self-Organizing Maps. The analysis is able to capture events with low and high low-cloud coverage. High-cloud coverage days are associated with cold-air outbreaks (CAOs). The combination of cold and dry conditions gives rise to an enhancement of surface heat fluxes during CAO, consistent with an increase in cloud fraction. In addition, prevailing winds during CAO days explain the occurrence of a synoptic maximum in cloud droplet number concentration, linked to transport of continental aerosol over the ocean. Overall, the dynamics of midlatitude low clouds substantially differ from archetypal stratocumulus clouds regimes.

1. Introduction

Marine boundary layer (MBL) clouds have been a topic of active research during recent decades owing to their central role in the Earth's energy budget (Hartmann et al., 1992). Their occurrence is preferentially over the global ocean, with distinct local maxima in cloud coverage located off the western edge of the continents in

the subtropics and in the baroclinic zonal bands of the extratropics (Wood, 2012). While low-altitude clouds in the extratropics are generally less persistent, broad stratiform cloud fields are easily identified in satellite imagery, in connection with midlatitude weather systems (e.g., Naud et al., 2014) and associated with rapid transitions in large-scale wind, surface fluxes, and temperature advection. Indeed, satellite climatologies reveal extensive cloud decks over the Southern Ocean as well as the midlatitude Pacific and Atlantic Oceans. Extratropical low clouds have recently drawn attention of the climate community due to their contribution to global cloud feedback in the Coupled Model Intercomparison Project Phase 6 (CMIP6) models, with a stronger feedback in the extratropics than in the tropics (Zelinka et al., 2020). As processes that control extratropical MBL cloud variability remain to some degree unexplored, the mechanisms that need to be refined in climate models for achieving a more faithful representation of low clouds, regionally and globally, are not well known. For instance, Naud et al. (2019) found a climate model underestimation of low-cloud cover in the postfrontal region in the Southern Ocean, which also extends to underestimations of Modern-Era Retrospective analysis for Research and Applications, version 2 (MERRA-2) and ERA-Interim reanalyses relative to satellite data (Naud et al., 2014). Challenges in simulating boundary layer clouds by climate models are also documented for the western North Atlantic Ocean (WNAO), where four climate models developed by U.S. research centers simulate a broad range in cloud cover and liquid water path (LWP) that differ from satellite climatologies (Painemal, Corral, et al., 2021).

Given the modulation of midlatitude weather disturbances in the evolution of clouds, a more in-depth characterization of extratropical low clouds and their representation in numerical models can be connected to our ability of identifying synoptic modes of variability. Moreover, an improved understanding of cloud–meteorology covariations is essential for isolating and quantifying aerosol effects on clouds and precipitation. These motivations call for methods of categorizing dominant modes of synoptic variability.

The WNAO is a region combining several climatological features of interest for the study of midlatitude boundary layer clouds. The strong baroclinicity favors the development of extratropical cyclones and associated cloud systems (e.g., E. K. M. Chang et al., 2002; Houze, 2014). The occurrence of cold-air outbreaks (CAOs) in winter (and its shoulder seasons) gives rise to stratiform clouds in postfrontal conditions (e.g., Fletcher et al., 2016), and episodic transport of continental aerosols over the adjacent ocean (Chin et al., 2007) likely modulates cloud microphysics and precipitation. Another key characteristic of the WNAO is the strong air–sea interactions across the warm sea-surface temperature (SST) of the Gulf Stream (Painemal, Corral, et al., 2021). While previous studies have highlighted cloud formation and boundary layer development associated with the extratropical cyclone passage (e.g., Grossman & Betts, 1990; Holt & Raman, 1990), the synoptic evolution of cloud fields during the passage of midlatitude weather disturbances has not been documented in a climatological context, to the best of our knowledge. The synoptic environment is central for understanding the mechanisms that control the lifecycles of stratiform cloud decks and the role of the atmospheric circulation in aerosol–cloud–radiation interactions. This characterization is also expected to be relevant for evaluating climate models and helping to disentangle effects attributed, for instance, to the response of the atmospheric boundary layer from those associated with the simulated atmospheric circulation. In this study, we endeavor to characterize the synoptic evolution of the winter circulation and cloud variability employing a pattern classification based on Kohonen’s Self-Organizing Map (SOM; Kohonen et al., 1996) applied to daily geopotential height fields at 600 hPa using a 12-year period (2009–2020). In addition, in situ observations collected during NASA’s Aerosol Cloud meteorology Interactions over the western Atlantic Experiment (ACTIVATE, Sorooshian et al., 2021) field campaign are used to provide a more detailed description of the aerosol and cloud properties typical of the synoptic regimes. Our goal is to provide a comprehensive description of the atmospheric and thermodynamic conditions that regulate the formation of low clouds, and the potential implications for the study of aerosol–cloud–meteorology interactions in the extratropics.

2. Data Set

The data are composed of 12 years of satellite and reanalysis data products for the 2009–2020 period and in situ airborne observations for the January–March (JFM) trimester, characterized by a peak in cyclonic activity. The data sets are briefly described below.

2.1. Satellite Observations and Reanalysis Data

Satellite cloud optical properties are taken from the MODerate resolution Imaging Spectroradiometer (MODIS) onboard the Aqua satellite, derived with the algorithms for the Cloud and the Earth’s Radiant Energy System (CERES) Edition 4 (Minnis et al., 2021, and references therein). Cloud retrievals include cloud areal fraction,

optical depth, droplet effective radius, top temperature and height, and liquid and ice water paths. These cloud properties are part of the Single Scanner Footprint (SSF) Edition 4 Level 3 product. Notably, SSF Level 3 is produced using 1-km nadir resolution retrievals and averaged within regular $1^\circ \times 1^\circ$ grids according to their cloud top pressure into four vertical levels. A low-cloud category with cloud tops below the 680-hPa level is included, following the definition of the International Cloud Climatology Project (Rossow & Schiffer, 1999). Pixel-level CERES-MODIS retrievals have been evaluated over the North Atlantic in Painemal, Spangenberg, et al. (2021) using data collected in the North Atlantic Aerosol and Marine Ecosystem Studies (NAAMES). Painemal, Spangenberg, et al. (2021) show good agreement between CERES-MODIS cloud droplet effective radius and optical depth and NAAMES measurements, with linear correlation coefficients up to 0.77, indicating that CERES-MODIS is a suitable data set for investigating cloud variability over the study region. The computation of cloud droplet number concentration (N_d) follows an adiabatic formulation, which is expressed in terms of cloud droplet effective radius, optical depth, temperature, and pressure as in Painemal (2018).

In addition to CERES-MODIS, we take advantage of satellite microwave LWP and rain rate from Remote Sensing Systems (RSS), derived at 0.25° grid resolution (Wentz & Meissner, 2007). To be temporally consistent with Aqua, we analyze retrievals from the Advanced Microwave Scanning Radiometer for Earth Observing System (AMSR-E, RSS Version 7) on Aqua (before 2012), and the Advanced Microwave Scanning Radiometer 2 (AMSR2, RSS Version 8) on the GCOM-W1 satellite (after 2011).

Daily meteorological fields at 18 UTC for 2009–2020 are taken from the NASA's MERRA-2 (Gelaro et al., 2017) and gridded to the resolution of CERES-MODIS Level 3 product. Seethala et al. (2021) found that MERRA-2 thermodynamical profiles capture the main features observed by dropsondes during the 2020 deployment phase of ACTIVATE campaign. Daily latent and sensible surface fluxes over the ocean correspond to the Objectively Analyzed Air-sea Fluxes (OAflux; Yu & Weller, 2007) at $1^\circ \times 1^\circ$ grid resolution.

2.2. ACTIVATE In Situ Data

ACTIVATE in situ observations collected during five continuous days of measurements in February–March 2020 (Deployment 1 of 6) were added to the satellite analysis. ACTIVATE is a multiyear field campaign (2020–2022) over the Atlantic Ocean, adjacent to Virginia coast in the U.S., based in NASA Langley Research Center (37.05°N 76.3°W). The ACTIVATE campaign consists of the deployment of two aircraft flying in formation. A low-altitude aircraft (Falcon) samples within the boundary layer and in the lower troposphere (below, above, and in the cloud layer). A high-altitude aircraft (King Air) flies about ~ 9 km above sea level and is equipped with remote sensors that allow for the derivation of aerosol and cloud properties, and a dropsonde system for characterizing the thermodynamics of the middle and lower troposphere. In this study, we make use of in situ observations collected by the Falcon aircraft (low altitude). More specifically, cloud droplet number concentration is computed from the droplet size distribution derived from the Fast Cloud Droplet Probe (FCDP, Knop et al., 2021). The FCDP, manufactured by SPEC Inc., is a forward scattering probe that measures droplet size distributions ranging from 1.5 to 50 μm (Kirschler et al., 2022). In addition, aerosol concentration in the range 90–7,500 nm is derived from the TSI Laser Spectrometer (LAS, Moore et al., 2021) model 3340. Aerosol and cloud microphysical data are complemented with thermodynamical profiles derived from dropsondes launched from the King Air (high-altitude aircraft).

3. Methodology: Synoptic Classification

During the past three decades, the SOM or Kohonen's SOM (Kohonen, 2014; Kohonen et al., 1996) has gained increasing popularity in climate research for the automatic classification of atmospheric patterns (e.g., L.-C. Chang et al., 2020; Gibson et al., 2017; Hewitson & Crane, 2002; Welty & Zeng, 2021). SOM is, for the purpose of this work, an unsupervised clustering technique that allows for the visualization of common features in a data set. More specifically, the SOM algorithm maps high dimensional data into specific orderly patterns and is particularly appealing for identifying synoptic variations and evolution of meteorological fields (e.g., Berkovic, 2017; Hewitson & Crane, 2002; Nishiyama et al., 2007). Briefly, the SOM algorithm arranges the data in a network of finite nodes in which the proximity between nodes is associated with their degree of similarity. Each node is characterized by a model, which corresponds to a smoothed vector (map) that represents a subset of the original data set (in our case, a collection of meteorological fields). The SOM training, or learning process, consists of

iteratively finding the “winner” models that best match the input data set. This is done by first constructing an initial model (for instance, an arbitrary daily map taken from the data set to be classified), which is iteratively tuned by means of a distance function between the model and the input data. Once the models are recursively computed, each input parameter can be assigned to a unique model and, thus, classified by minimizing the distance between the input and model maps. A main distinction between SOM and other classification techniques is that the SOM algorithm yields smooth models (patterns) and during the iterations toward constructing a model, the neighboring models in the network are also simultaneously updated. In other words, neighboring SOMs are mathematically linked through the training process. Regarding the number of nodes, methods exist for estimating the optimal number that represent the diversity of the observed data set. The purpose of this analysis is to capture general synoptic features, rather than identifying all the nuances of the spatial variation, and thus we make the analysis tractable by a priori defining 15 nodes. For simplicity, we used a rectangular network of 3×5 nodes, which SOM uses to define the neighborhood relationship between nodes. We also computed 4×5 SOM (not shown), however, given additional postprocessing explained later, the final classification is minimally affected by the configuration used by the algorithm. We use a MATLAB-based SOM code developed by Helsinki University of Technology (Kohonen, 2014). The code initializes the models based on principal component analysis when possible, otherwise the initialization is done random. The SOM training is given by a Gaussian neighborhood function, its radius, and learning rate. Briefly, the neighborhood function establishes the relationship between adjacent nodes. The SOM training is performed in two phases: coarse and fine training, with each phase characterized by specific neighborhood radius and learning rate. The reader is referred to Kohonen (2014) and Vesanto et al. (1999) for more details of the SOM algorithm. Here, we use “som_make” of the Helsinki University of Technology’s MATLAB package, which handles the selection of multiple parameters in an automated manner following the steps previously described.

The SOM methodology in our study is similar to that in Mechem et al. (2018) and is based on geopotential heights (ϕ) at 600 hPa and is qualitatively similar to those using the 500 hPa level (not shown). ϕ is first deseasonalized by subtracting its 30-day running mean for each grid point. We further normalize the fields by their 30-day running standard deviation to reduce the weight of strong daily events on the pattern classification and to prioritize the classification of spatial patterns. An area correction based on the cosine of latitude is also included, yet its effect is modest.

The SOM constructed from 12 years of daily MERRA-2 ϕ for the JFM trimester is depicted in Figure 1. The advantage of the SOM approach is evident, as the algorithm is able to orderly organize the fields in such a way that the typical evolution of the baroclinic wave can be easily identified. This is particularly clear for the upper row in Figure 1 (SOM 1, 4, 7, 10, and 13) and, in general, for adjacent SOMs. Next, each daily map is assigned to one of the 15 SOMs in Figure 1 through distance minimization. Figure 2 depicts composites (contours) and anomalies (colors) of 600-hPa geopotential height for JFM associated with each SOM shown in Figure 1. The ϕ composites and anomalies in Figure 2 (black contours and colored shades, respectively) are analogous to the SOMs in Figure 1, with differences attributed to the data normalization used to train the SOM. Again, the evolution of the wave train is well identified in the composites, especially for the first sets of SOMs in Figure 2 (SOM 1, 4, 7, 10, and 13). This SOM clustering already allows for the study of synoptic processes over the region of study, however, to facilitate the extraction of quantitative information, methods exist for regrouping SOMs according to their level of similarity (e.g., Vesanto & Alhoniemi, 2000). A closer look at Figure 2 reveals the dominance of specific features: ridge, trough, ridge–trough transitions, and weak anomalies that minimally depart from the climatological mean. This motivates further regrouping of SOMs into five atmospheric patterns: ridge, trough, ridge–trough transition (westward ridge), trough–ridge transition (westward trough), and weak anomaly. To separate ridge and trough from their transitions, we use Bermuda Island as a point of reference (32.3°N , 64.8°W , triangle in Figure 3) and define ridge–trough and trough–ridge configurations (from west to east) when the change of anomaly sign (zero anomaly) is within 15° of Bermuda. If the transition is outside the 15° range, the map is classified as either dominant ridge or trough. Thus, SOMs are regrouped as follows: (a) SOM 10 and 13 as ridge, (b) trough for SOM 3 and 6, (c) ridge–trough for SOM: 1, 2, 4, and 7, (d) trough–ridge for SOM: 9, 12, 14, and 15, and (e) weak anomalies for SOM: 5, 8, and 11. The frequency of occurrence of each group and associated SOMs is listed in Table 1.

The five synoptic regimes are depicted in Figure 3 (upper panels). The contrast between the clusters is evident, with each of them representing archetypal stages of the baroclinic wave, with dominant ridge (Figure 3a) and trough (Figure 3b) cores located around the center of the domain, and a wave train that is manifested as

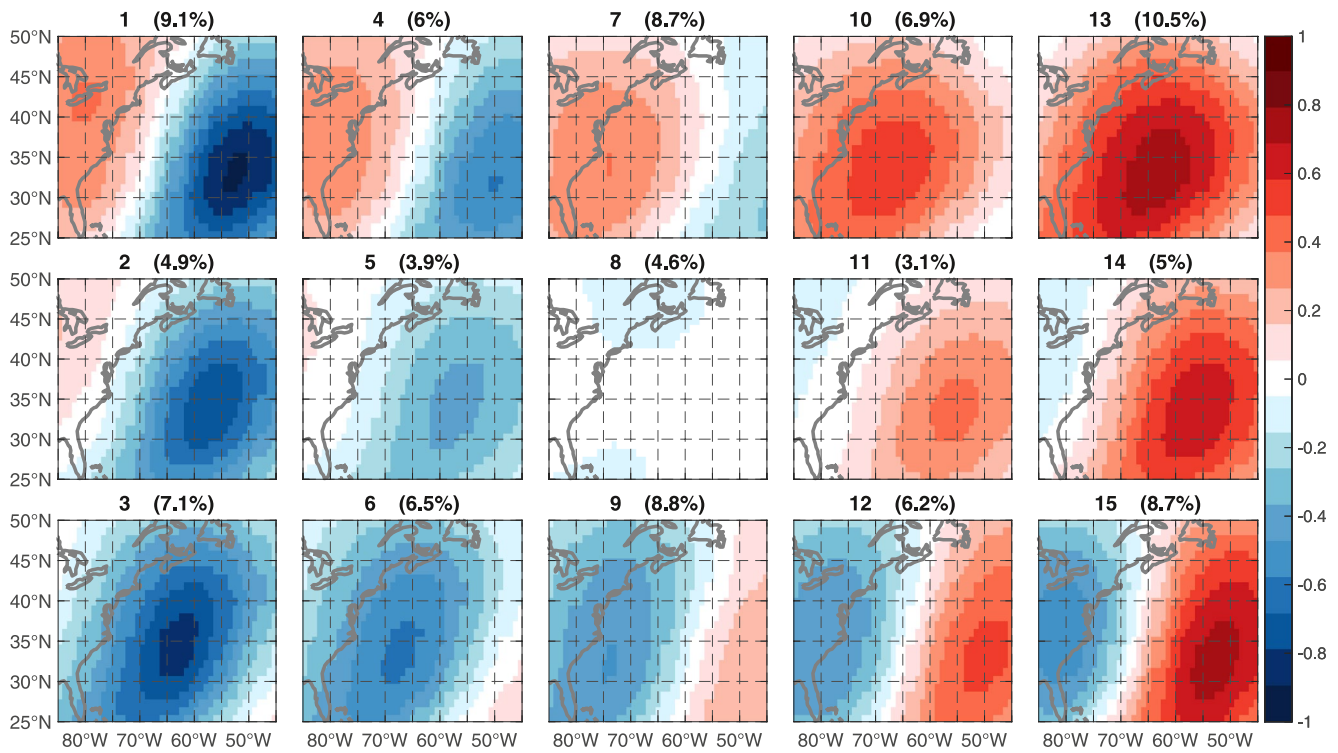


Figure 1. Self-Organizing Map (SOM) models estimated from normalized and deseasonalized geopotential height fields at 600 hPa using 12 years of winter months (January–March). Unlabeled signs represent anomalous ridge (positive) and trough (negative). Frequency of occurrence is denoted in %.

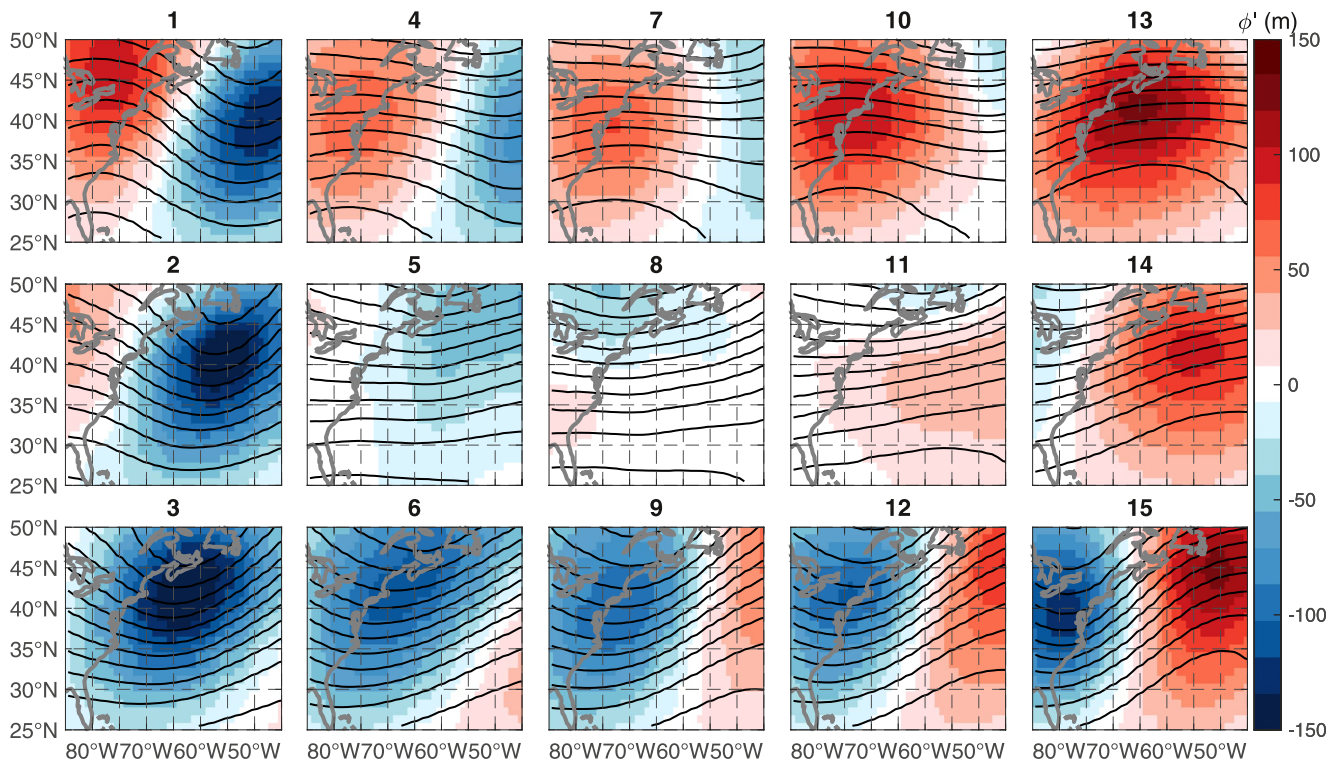


Figure 2. Composite fields of geopotential height (contours) and deseasonalized anomalies (color) associated with the 15 Self-Organizing Maps (SOMs) depicted in Figure 1.

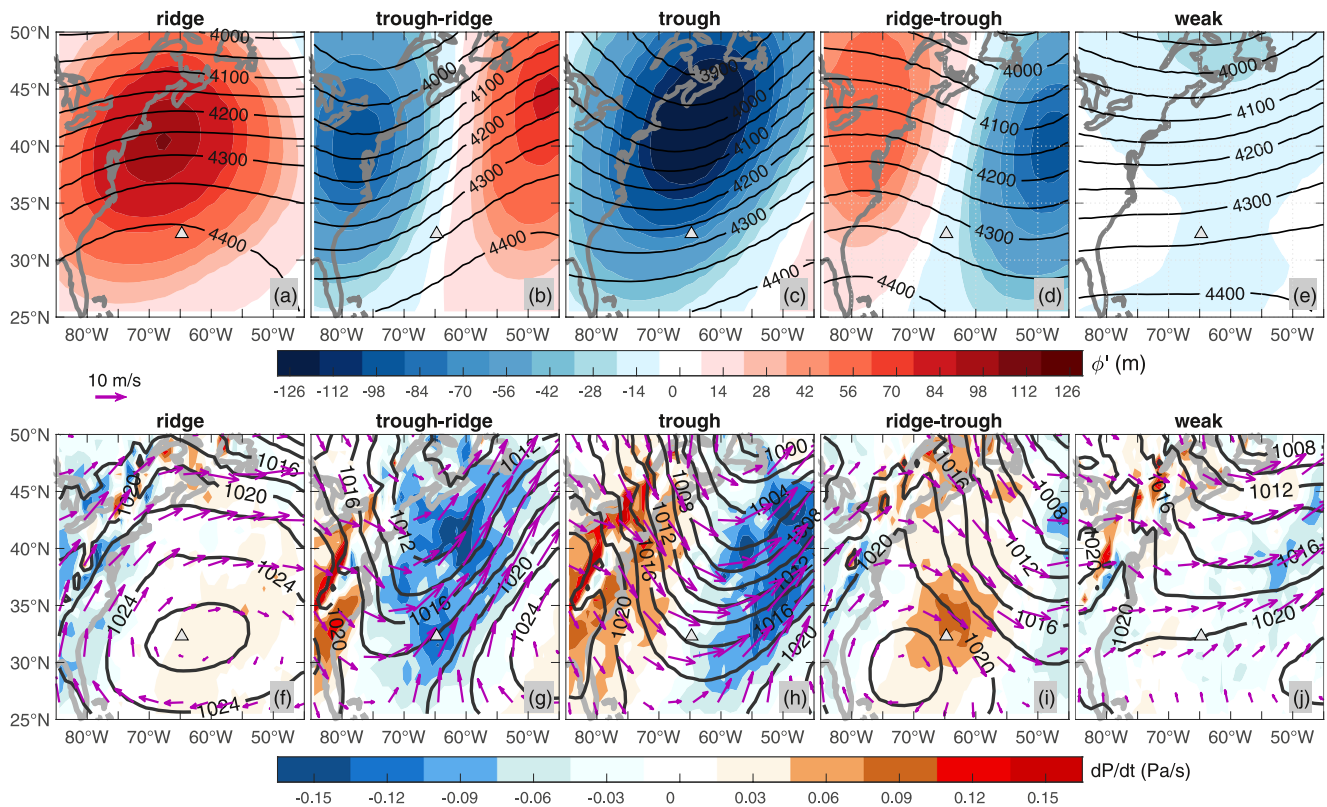


Figure 3. Upper panel: final synoptic classification based on Self-Organizing Map (SOM): (a) ridge, (b) trough–ridge, (c) trough, (d) ridge–trough, and (e) weak cluster. Lower panel: synoptic patterns based on the 600-hPa geopotential height in (a)–(e), composited in terms of sea-level pressure (contours), omega velocity at 600 hPa (color bar represents dP/dt , with P denoting the air pressure) with positive values denoting descent, and horizontal winds at 950 hPa (magenta arrows).

a continental trough and oceanic ridge (trough–ridge, Figure 3c), and a continental ridge and oceanic trough (ridge–trough, Figure 3d). The zero-anomaly zone for the trough–ridge and ridge–trough is approximately located around Bermuda (triangle) by design. In the following, we make use of these five clusters to describe the evolution of atmospheric circulation and clouds, with an emphasis on boundary layer clouds.

4. Results

4.1. Atmospheric Circulation and Surface Fluxes

Sea-level pressure, boundary layer winds (at 950 hPa), and large-scale vertical wind in pressure coordinates (omega: dP/dt) at 600 hPa composited as a function of the occurrence of ridge, trough–ridge, trough, and ridge–trough, and weak signal (modest departure from the climatological mean) are depicted in the lower panels of

Figure 3. Sea-level pressure for the four stages follows the expected evolution of midlatitude weather disturbances, with a dominant anticyclone (Figure 3f) associated with a geopotential height ridge (Figure 3a) that induces winds that blow parallel to the coast, which transition to westerlies north of 45°N. The presence of a low pressure for the trough–ridge (Figure 3g) is consistent with the pretrough area inducing strong ascent (omega < 0) and coastal northwesterlies that induce cold and dry advection over the ocean. As the trough strengthens, and the cyclone moves eastward, subsidence is observed along the coast (Figure 3h), the location of upward motions moves offshore, and northwesterly winds become stronger. Finally, the eastward displacement of the low pressure is followed by the development of an anticyclone over the western part of the domain, with descent over the preridge zone, 10° away

Table 1
Five Synoptic Regimes, Associated SOM Clusters, and Frequency of Occurrence During JFM

Synoptic regime	SOM groups	Occurrence %
Ridge	10, 13	17.4
Trough–ridge	9, 12, 14, 15	28.6
Trough	3, 6	13.6
Ridge–trough	1, 2, 4, 7	28.7
Weak anomaly	5, 8, 11	11.5

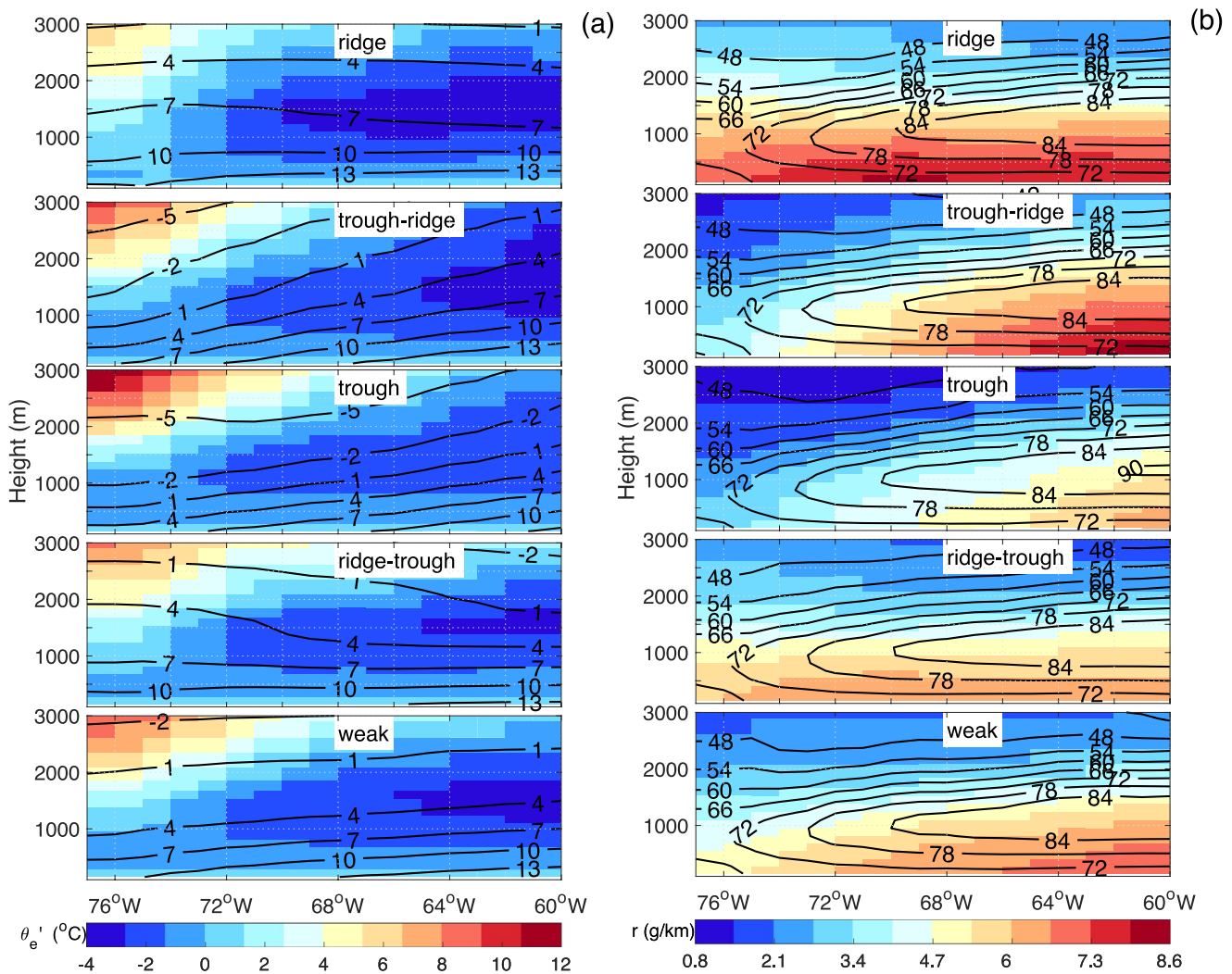


Figure 4. Zonal cross sections averaged over the 35°–40°N latitudinal band. (a) Equivalent potential temperature departures (θ_e') estimated as the equivalent potential temperature difference for each level and that at the sea surface. Black contours correspond to air temperature. (b) Water vapor mixing ratio (r , color) and relative humidity (black contours).

from the coast (see Figure 3i). The weak pattern is characterized by modest zonal winds and a smooth cyclonic circulation north of 30°N (Figure 3j).

The thermodynamical structure associated with each synoptic regime is shown in the zonal cross sections of Figure 4 for the 35°N–40°N mean latitudinal band. The trough–ridge and trough regimes feature low air temperatures (Figure 4a, black contours), with a synoptic minimum for the trough and below-zero temperatures in the boundary layer, driven by the cold advection attributed to the northerly winds (Figure 3h). In contrast, temperatures greater than 10°C below 500 m are typical for the ridge pattern, which is consistent with warm advection brought by the anticyclonic circulation. Equivalent potential temperature in Figure 4a (colors) is expressed in terms of departures from near-surface values (θ_e' , Figure 4a, colors) to simplify interregime comparisons. θ_e' reveals a temperature inversion for all the synoptic patterns confined to the coastal areas west of 70°W. Even though θ_e' differences are relatively modest, the strongest inversion is observed for the trough composite for heights above 2 km, likely influenced by coastal subsidence (Figure 3h). In terms of atmospheric humidity, the trough–ridge pattern initiates a shift toward a drier atmosphere, reaching the driest conditions for the trough, and followed by a humidity recovery during the ridge–trough, which is, again, in agreement with the wind patterns and transition from continental advection of dry air (ridge–trough and trough) to anticyclonic circulation (ridge). Finally, changes in relative humidity (Figure 4b, black contours) are modest, which reflects a compensation

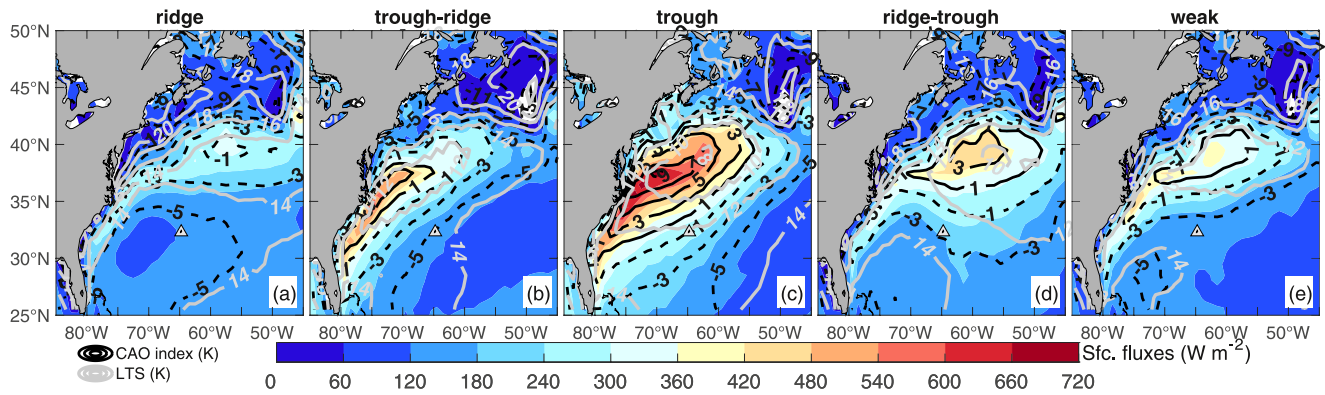


Figure 5. Oaflux surface heat flux for each synoptic pattern (colors). Cold-air outbreak index and lower tropospheric stability (LTS) correspond to black and gray contours, respectively. Negative cold-air outbreak (CAO) index is denoted with dashed lines.

between atmospheric drying and cooling effects. Overall, an inversion strengthening, dryness, and a rapid decrease in air temperature during the trough regime are typical of CAO events (e.g., Papritz, 2017).

Further characterization of the lower troposphere is obtained by means of combined sensible and latent surface heat turbulent fluxes from Oaflux, lower tropospheric stability (LTS) defined as the MERRA-2 potential temperature difference between 800 hPa and near-surface (2 m) levels, and the CAO index expressed as the potential temperature difference between the sea surface (skin) and 800 hPa (Fletcher et al., 2016; Figure 5). Surface fluxes are enhanced over the coastal region for the trough–ridge field, reaching a regional maximum ($\sim 700 \text{ W m}^{-2}$) for the trough, with an eastward extension up to 60°W with fluxes greater than 400 W m^{-2} . This dramatic synoptic maximum lends support to Shaman et al. (2010) who noted that CAOs are instrumental to explain a winter peak in latent and sensible heat fluxes for the WNAO. Indeed, using the simple identification of CAOs as samples with CAO index >0 (Fletcher et al., 2016), it becomes evident that the trough is the synoptic configuration more propitious for CAO occurrence, followed by the trough–ridge, and ridge–trough (Figure 5, black contours). The CAO index maps also show the evolution of the CAO events. These events originate near the coast, then strengthen and expand, and finally weaken as they move offshore. Interestingly, spatial and synoptic transitions of the CAO index maps closely follow those of the surface heat fluxes, with negative values associated with fluxes of less than 300 W m^{-2} , and a regional maximum during the trough. Lastly, LTS synoptic variations are small, with interregime variations of less than 4 K (Figure 5, gray contours). The modest LTS variation over these regions was also noted at seasonal scale by Sorooshian et al. (2019) and Painemal, Corral, et al. (2021). In sum, variations in surface heat fluxes can be interpreted in terms of the cyclone dynamics and the SST pattern. While the coastal minimum in surface fluxes north of 35°N is primarily explained by the colder SST near the coast, where the Gulf Stream detaches from the continental shelf (see Figure 1 in Painemal, Corral, et al., 2021; Painemal, Spangenberg, et al., 2021), near-surface winds (Figure 3, lower maps) drive advective changes over the domain. The anticyclonic circulation for the ridge pattern anticipates warm advection that yields a reduction in the air–sea temperature contrast, driving a minimum in surface fluxes. Coastal winds from the north and cold and dry advection accounts for an increase in surface fluxes confined to the coastal band for the trough–ridge. Similarly, a northerly wind strengthening for the trough regime, west of the cyclone core, gives rise to a synoptic maximum in surface fluxes (Figure 5c). With the eastward displacement of the cyclone for the ridge–trough, northerly winds (and cold advection) become dominant well offshore, and thus, accounting for an increase of heat fluxes east of 65°W .

4.2. Cloud Fields and Precipitation

MODIS cloud fraction (CF) for boundary layer clouds is computed as the number of pixels with cloud heights below 680 hPa to the total in a $1^\circ \times 1^\circ$ grid. Similarly, the combined midlevel and high-level CF is estimated as the fraction of pixels with cloud heights above 680 hPa relative to the total (equivalent to the difference between total and boundary layer CF). In terms of boundary layer CF (Figures 6a–6d, colors), the fields transition from a minimum in cloud coverage during the ridge, to increasing coastal values for the trough–ridge, reaching a CF peak for the trough composite. The regional maximum in cloud coverage moves eastward during the ridge–trough, with maxima far offshore. This CF displacement occurs with a similar eastward transition in the CAO index maps and surface fluxes depicted in Figure 5. Indeed, we find high spatial correlations between surface

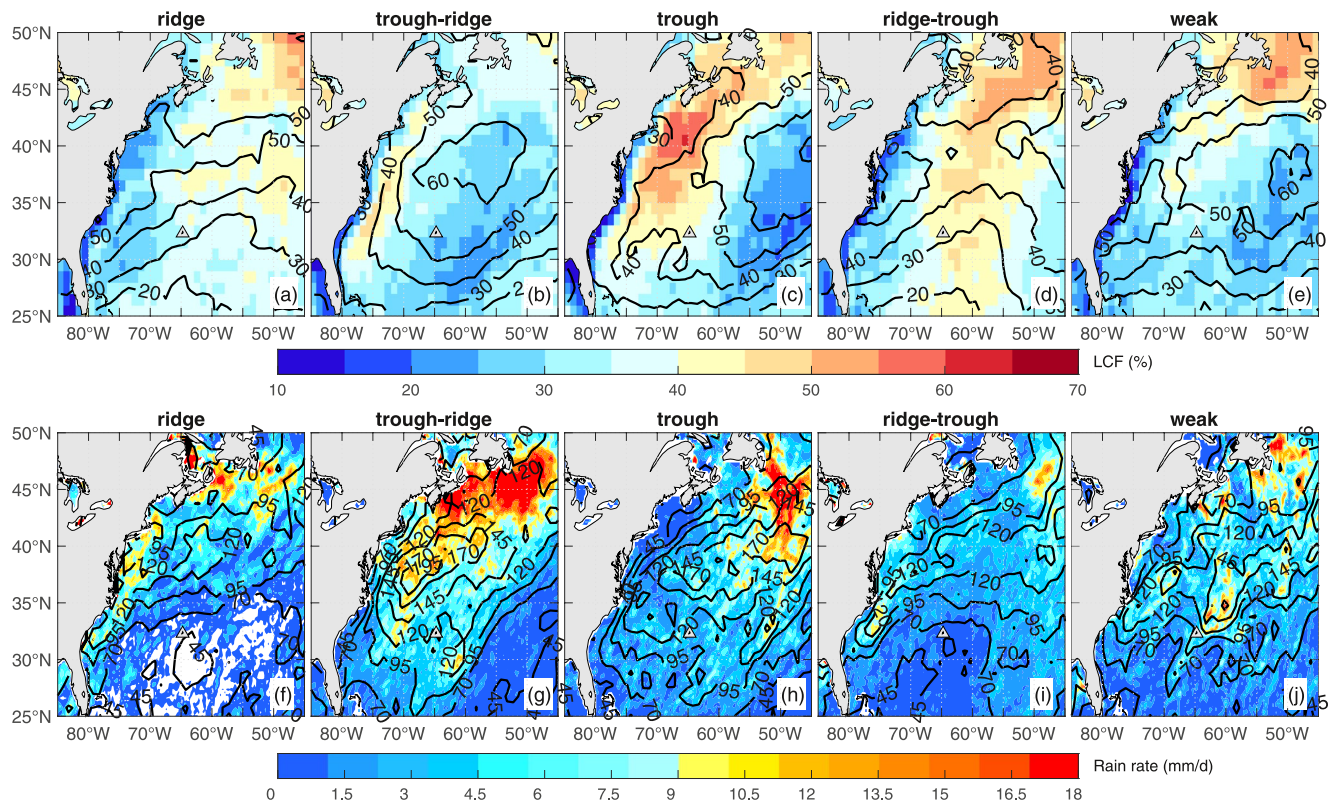


Figure 6. Upper panel (a–e): MODIS low-cloud fraction (colors) and midclouds and high clouds (contours) for each synoptic composite. Lower panel (f–j): AMSR-E/2 rain rate for nonzero rain rates (colors) and liquid water path (contours, in g m^{-2}) for the five synoptic regimes.

heat fluxes and CF south of 41°N , with linear coefficients of 0.45 (ridge), 0.66 (trough–ridge), 0.77 (trough), 0.55 (ridge–trough), and 0.55 (weak anomalies). Positive correlations between the CAO index and CF were also reported for the winter months by Painemal, Corral, et al. (2021), with reported temporal linear correlations ranging between 0.4 and 0.5. For the region north of 41°N in Figure 6, a relationship between fluxes, CAO index, and CF is unclear. Middle and high clouds are pervasive over the region, with percentage coverage from 20% to 60%. A maximum mid/high-cloud coverage of 60% is centered at 60°W and 38°N for the trough–ridge, which is the likely manifestation of frontal convective activity, as indicated by the upward motion in Figure 4b. Lastly, a local minimum in cloud coverage is observed along the coast. This reduced coastal CF is primarily contributed by cloud-free days (not shown), over a coastal area dominated by near-surface wind divergence, reduced surface heat fluxes, and colder SST (Painemal, Corral, et al., 2021; Painemal, Spangenberg, et al., 2021). The coastal area is also affected by the dryer land-based air mass with offshore winds in CAOs.

AMSR-E/AMSR2 rain rates for the synoptic fields in Figures 6f–6j (color) feature a maximum of 18 mm/day north of 40°N for the trough–ridge composite, over the region with strong upward motion, east of the cyclone core, in agreement with Field and Wood (2007). As the ascent region moves eastward, rain peaks far offshore for the trough composite. A substantial decrease in rain rate for the ridge–trough is concomitant with the dominant presence of marine low clouds east of 65°W . LWP (Figures 6f–6j, contours) is also a synoptic maximum during the trough–ridge regime west of 60°W (195 g m^{-2}) and slightly south from the rain rate peak in Figure 6g, a mismatch likely explained by the presence of ice clouds in the active convective region farther north, which are undetected by the microwave product.

Cloud droplet number concentration (N_d) of low clouds from Aqua-MODIS shows regional peaks near the coast, as previously reported in Sorooshian et al. (2019), Painemal, Corral, et al. (2021), and Dadashazar et al. (2021), whereas values remain below 50 cm^{-3} east of 60°W (Figure 7, color). Coastal N_d ranges between 110 and 230 cm^{-3} , with synoptic maxima for the trough–ridge and trough composites ($N_d > 200 \text{ cm}^{-3}$). In contrast, low N_d occurs during the ridge and ridge–trough types, under the dominance of the anticyclone ($N_d < 150 \text{ cm}^{-3}$, Figure 9a). These transitions between high and low N_d are concomitant with near-surface winds that favor aerosol advection

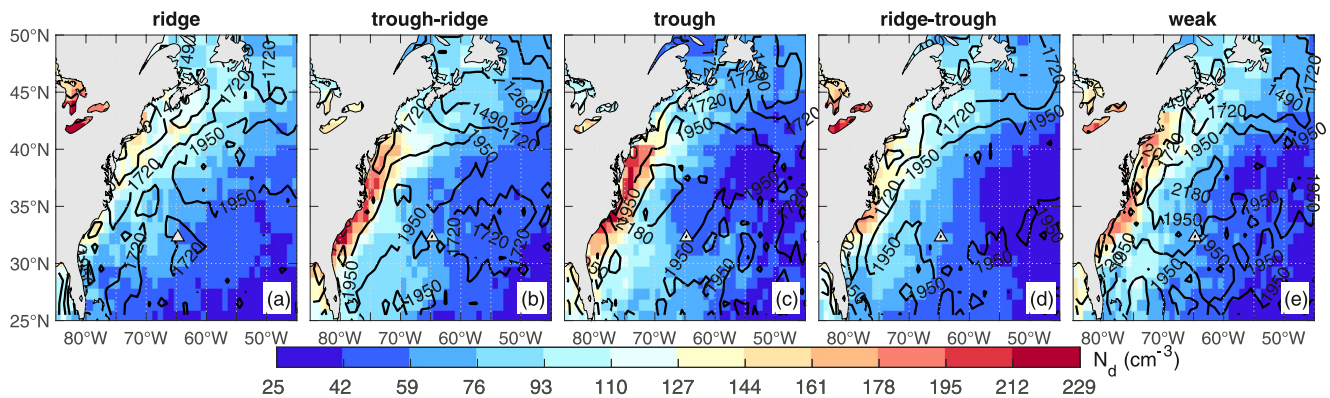


Figure 7. CERES-MODIS cloud droplet number concentration (N_d , color) and cloud top height (contours in m) for the five synoptic regimes in winter.

of continental and maritime aerosols, respectively. In terms of cloud top height (Figure 8, black contours), mean values are generally above 1,600 m, with slightly deeper clouds for the trough regime (2 km).

To understand the link between aerosol variability and N_d , MERRA-2 speciated aerosol optical depth (AOD) is composited into the five synoptic clusters. We simplify the analysis by separately considering sea salt and nonsea salt species with anthropogenic origin (organic carbon, black carbon, and sulfate). Dust is excluded from the analysis as its contribution to AOD is negligible in winter (Dadashazar et al., 2021). In terms of sea salt (Figure 8, color), the main AOD changes are featured over the open ocean, with a maximum for the trough, followed by the trough–ridge, as expected from the near-surface wind speed enhancement (Figure 3, lower maps). Anthropogenic AOD shows similar magnitudes as that for sea salt, ranging between 0.04 and 0.1, and with a clear eastward decrease (Figure 8, contours). Interregime differences for pollution AOD are, nevertheless, modest and dissimilar to the interregime changes in coastal N_d .

4.3. Airborne Observations During ACTIVATE

We take advantage of 5 days of consecutive observations during ACTIVATE in the winter of 2020 for the period between 27 February and 2 March to provide a more detailed characterization of the synoptic regimes. This is particularly relevant as MERRA-2 atmospheric fields and MODIS cloud properties are less suited for describing aerosol concentration, cloud condensation nuclei (CCN), and the vertical structure of the boundary layer. Moreover, applying the SOM-based classification to the ACTIVATE data set provides a test of skill for identifying specific meteorological patterns in large data sets such as CAO events, cyclones, and anticyclones. 27 February was characterized by a 600-hPa trough–ridge configuration, low pressure over the land–sea interface, and ascents ($\omega < 0$) associated with a cold front (Figures 9a and 9b). The trough–ridge moved eastward on 28 February and the low pressure weakened and moved northward. The eastward displacement of the ridge away from the region of study and the dominance of the trough axis became more evident on 29 February, with subsidence developing over the

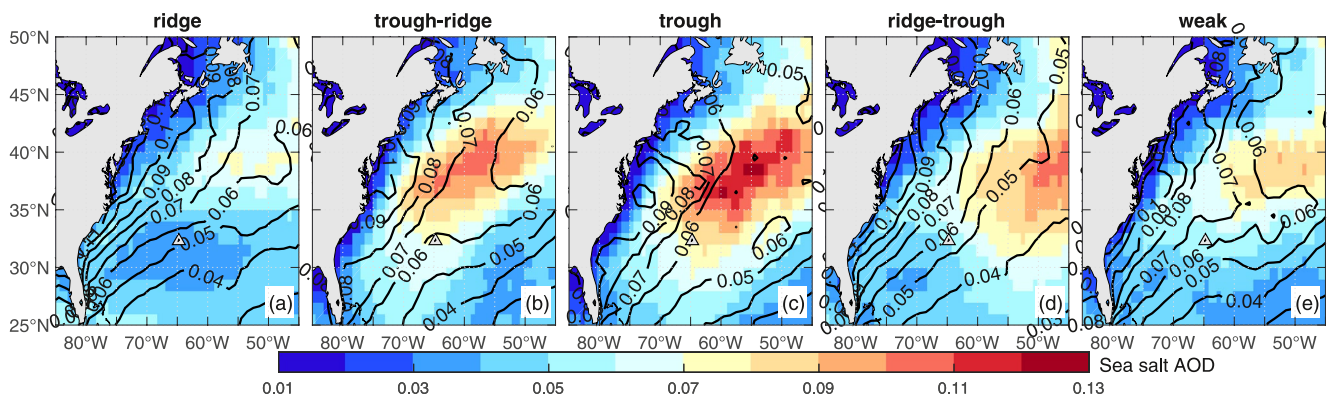


Figure 8. MERRA-2 speciated aerosol optical depth (AOD) for the two primary contributors to total AOD: sea salt (colors), and the combined AOD from sulfate, organic carbon, and black carbon (contour).

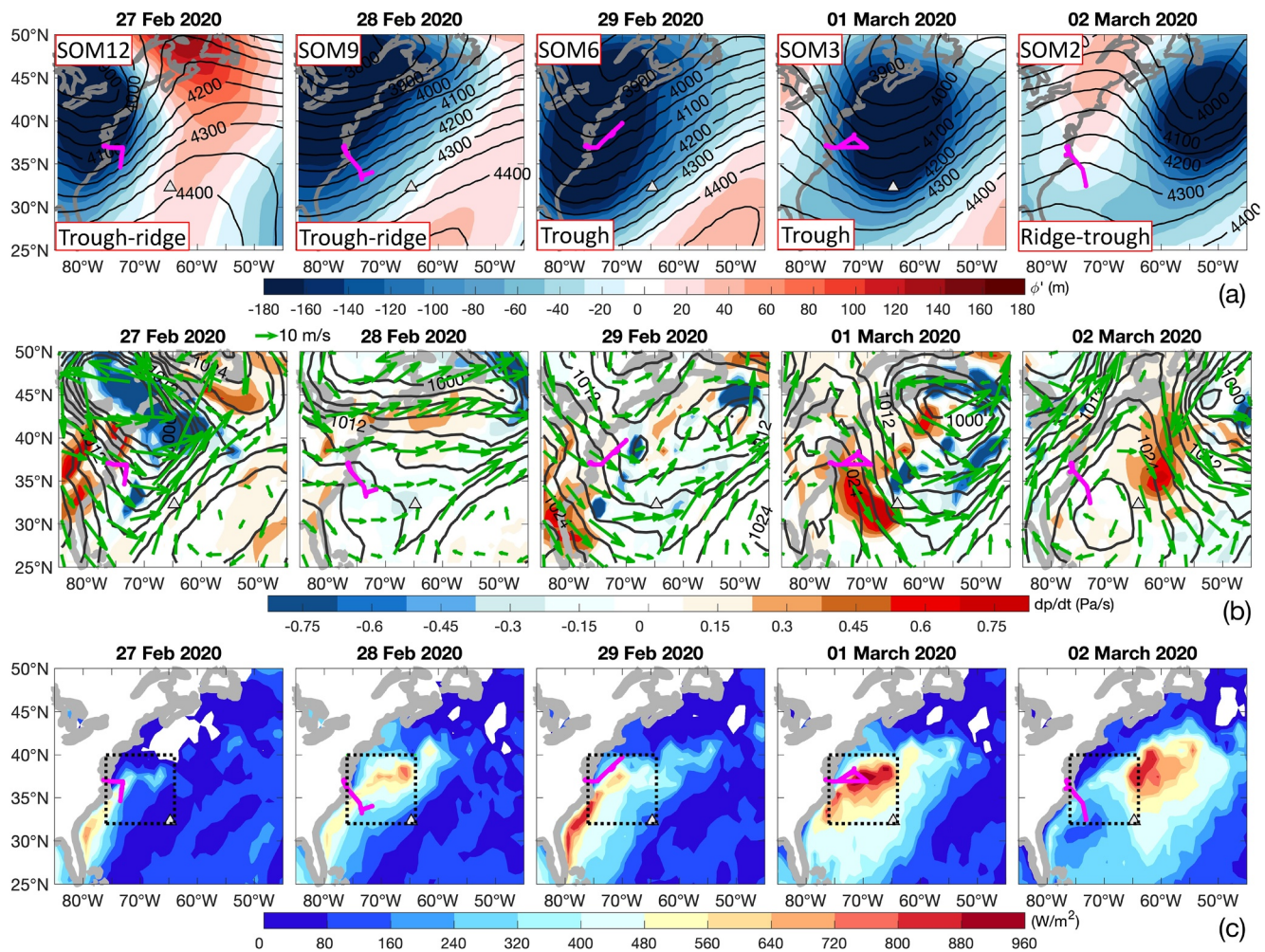


Figure 9. Regional maps for five continuous days sampled during ACTIVATE 2020 (27 February to 2 March period): row (a) geopotential height at 600 hPa (contours) and anomalies (colors); (b) sea-level pressure (black contours), omega velocity at 600 hPa (color) and boundary layer wind vectors (green arrow); (c) surface heat fluxes. Magenta lines represent the Falcon aircraft track.

southwestern edge of the domain (Florida). On 1 March, the trough was the main feature in the midtroposphere, with an anticyclone in the west and subsidence over the ocean south of 40°N. The contrast in large-scale vertical wind between 28 February and 1 March was also noted by Li et al. (2022) who found strong subsidence up to -8 cm s^{-1} on 1 March and weak ascending flow for 28 February ($\sim 2 \text{ cm s}^{-1}$). Finally, a ridge–trough pattern moved over the region on 2 March, with an anticyclone that covered most of the western domain. The SOM classification and the postclassification described in Section 3 (upper left box in Figure 9a) for the ACTIVATE days are SOM 12 (trough–ridge) for 27 February, SOM 9 (trough–ridge) for 28 February, SOM 6 (trough) for 29 February, SOM 3 (trough) for 1 March, and SOM 2 (ridge–trough) for 2 March. This SOM-based classification correctly captures the features described above. Finally, a progressive increase of OAflux surface heat fluxes that reach a synoptic maximum for the trough pattern on 1 March (Figure 11c) is consistent with the SOM analysis. These strong fluxes, combined with cold advection and subsidence on 1 March, are features that favor the occurrence of postfrontal clouds as discussed in Section 4.2. Lastly, with the eastward displacement of the trough on 2 March and the presence of a ridge–trough transition, warm advection driven by the anticyclonic circulation inhibits the generation of surface heat flux near the coast. On the other hand, northerly winds (and cold advection) east of 65°W promote heat flux enhancement offshore on 2 March, again, in agreement with the ridge–trough analysis in the previous section.

Before presenting the ACTIVATE in situ observations, we briefly discuss the cloud fields during the 5-day period through liquid and ice water paths derived from the 16th Geostationary Operational Environment Satellite (GOES-16) at 18 UTC (~ 13 local time) and produced by NASA Langley Research Center (e.g., Painemal, Spangenberg,

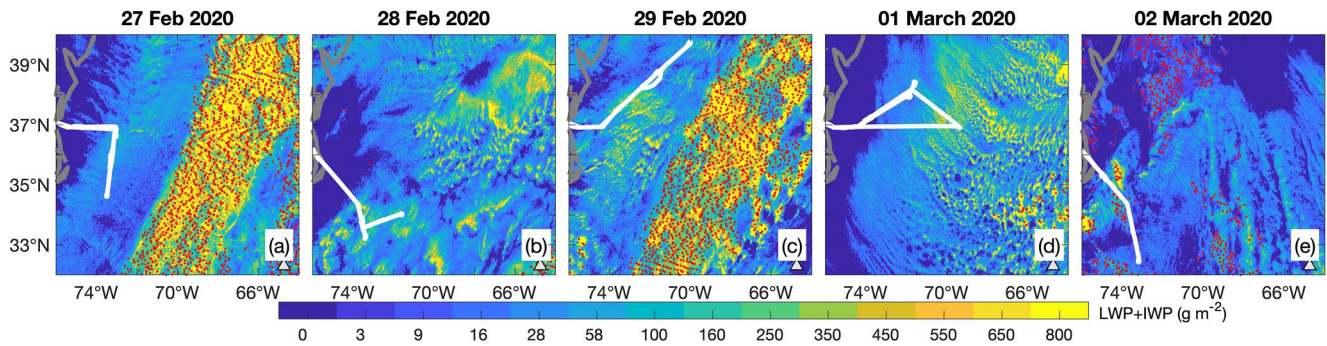


Figure 10. GOES-16 retrievals of total (liquid + ice) vertically integrated condensate at 18 UTC (~13 local time) over the flight domain of the five days of ACTIVATE flights, with white lines showing aircraft tracks. Regions with red dots represent cloud with tops higher than 4 km. Note the different domain size with respect to Figure 9.

et al., 2021). Condensed water path maps in Figure 10 reveal broad regions with stratiform clouds that were sampled by the aircraft, with convection observed on 27 and 29 February (red dots) away from the aircraft track. As discussed by Li et al. (2022), the cloud field on 1 March, capped by a strong subsidence, corresponds to a well-organized closed-cell deck, with cloud clusters exhibiting LWP greater than 500 g m^{-2} . In contrast, low LWP ($<100 \text{ g m}^{-2}$) and more disorganized clouds were observed on 2 March. This reduced condensed water path and more broken conditions on 2 March relative to other days is also captured by the synoptic pattern composites, which evince a decrease in cloud water content for the ridge–trough pattern relative to both trough and trough–ridge (Figure 8, contours).

Daily averaged thermodynamical profiles derived from dropsondes are depicted in Figure 11. Equivalent potential temperature (θ_e) features lower temperature during the trough days (29 February and 1 March, red and magenta), with surface temperatures more than 8 K below preceding and following days. This temperature drop, characteristic of a CAO, is also to some extent observed in the climatological composites of Figure 4. θ_e profiles show weak temperature inversions above 850 hPa, except for 1 March, and a well-mixed boundary layer below 870 hPa. Profiles of relative humidity show modest variations in the boundary layer; however, a much drier boundary layer (lower mixing ratio) was observed for the trough days (29 February and 1 March), again, in agreement with the MERRA-2 analysis depicted in Figure 4b. In sum, the synoptic trough is the archetypal pattern of the CAO in the WNAO. Next, we describe the aerosol and cloud properties for the same 5-day period.

Zonally averaged accumulation-mode aerosol concentration—sizes greater than $0.1 \mu\text{m}$ —for cloud-free samples below 1-km flight level (N_a , Figure 12a) is the greatest for 29 February and 1 March, that is, for the days identified as trough and associated with CAOs. 29 February departs from 1 March in that the concentrations are relatively

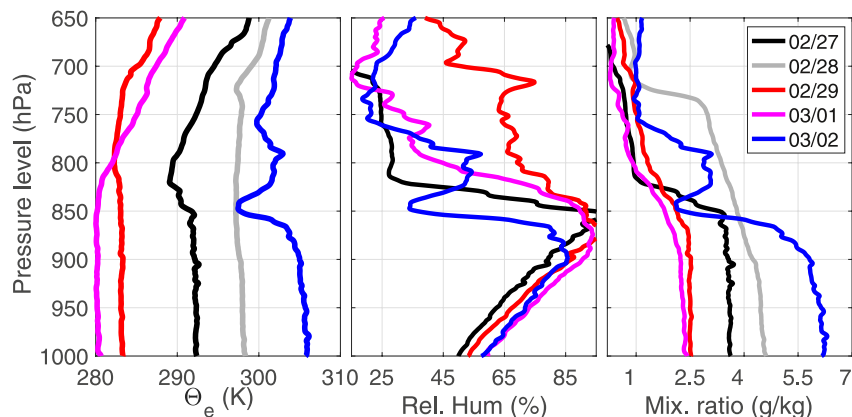


Figure 11. Mean thermodynamical profiles from dropsondes for the five winter days during ACTIVATE 2020.

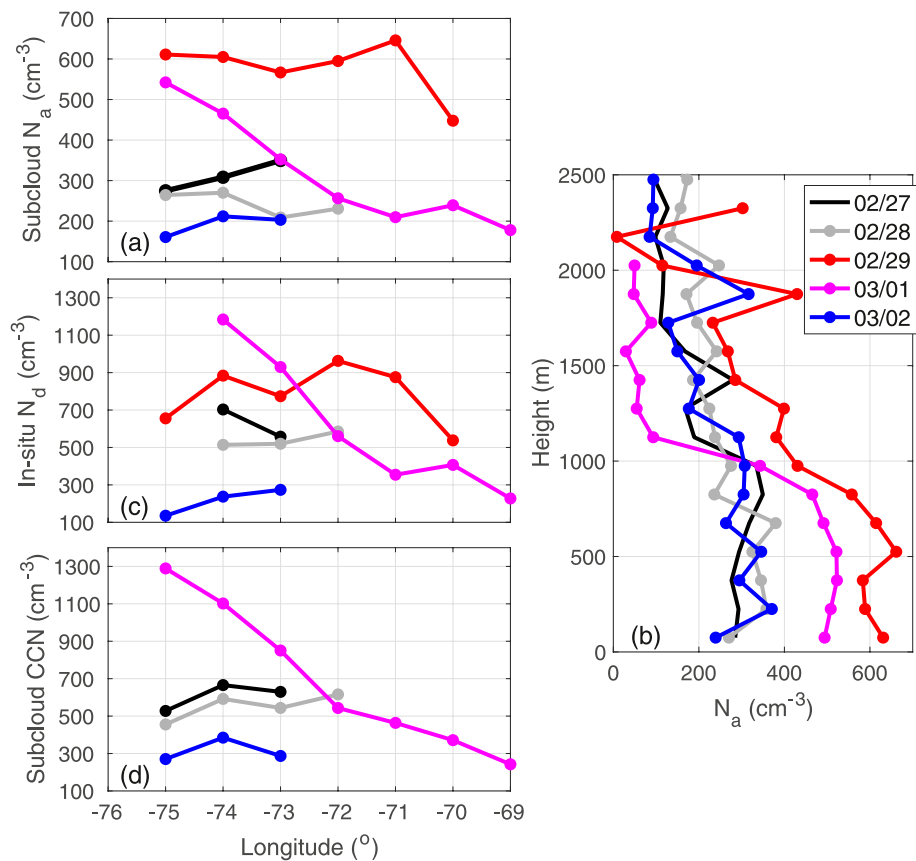


Figure 12. In situ observations collected over five continuous winter days during ACTIVATE 2020. (a) Accumulation aerosol concentration ($>0.1 \mu\text{m}$) below 1,000 m binned in 1° longitudinal bands. (b) Vertical profiles of accumulation-mode aerosols for cloud-free samples west of 72.5°W . (c) Cloud droplet number concentration binned in 1° longitudinal bands. (d) As in a but for cloud condensation nuclei (CCN) concentration at 0.3%–0.4% supersaturation below 1,000 m binned in 1° longitudinal bands. February 27 (black), 28 February (gray), 29 February (red), 1 March (magenta), and 2 March (blue).

constant with longitude, suggesting an active aerosol transport from the continent, as indicated by the boundary layer winds inland and over the ocean (Figure 9b, green arrows). We describe the aerosol vertical structure by first binning N_a in 100-m vertical intervals for observations collected over the zonal range that was sampled by all five flights (west of 72.5°W , Figure 12b). N_a vertical profiles show that while concentrations are large for both 29 February and 1 March flights, the large N_a values are confined to the layer below 1,200 m on 1 March. This feature is possibly associated with subsidence that prevents the aerosol transport to higher elevations on 1 March (Figure 9b, colors).

Zonal variations of cloud droplet number concentration tend to follow the same pattern as N_a , with 29 February and 1 March presenting the highest N_d , but with a rapid eastward decrease during 1 March (Figure 12c). It is worth noticing that N_d magnitudes are substantially larger than those for N_a , implying that aerosol activation occurred on particles smaller than 100 nm. Indeed, the observed CCN concentration at 0.3%–0.4% supersaturation is consistently greater than N_a by about 200 cm^{-3} , with concentrations similar to N_d (Figure 12d). Unfortunately, the lack of CCN data during 29 February prevents us from a more detailed CCN analysis.

5. Discussion

Conventional methods for constraining meteorological variability of aerosol–cloud–meteorology interaction studies typically rely on data stratification of aerosol and cloud properties as a function of one or more atmospheric parameters, such as lower tropospheric stability or subsidence (e.g., Su et al., 2010). The pitfall of such

an approach is that cloud and aerosol variability are controlled by weather and large-scale patterns, which are manifested at spatiotemporal scales that cannot be fully captured with a binning technique, which is generally applied to individual grid sizes independent of the surrounding grids and meteorological history. In addition, covariation of multiple meteorological parameters makes use of several meteorological control parameters an ineffective way to understand the role of the atmospheric circulation on cloud and aerosol properties. In contrast, meteorological clustering provides an alternative framework that better integrates regional-scale phenomena with cloud variability. The clustering method is particularly successful at finding modes of variability in cloud coverage, surface fluxes, and wind fields.

Strong surface forcing is a key difference of these low clouds compared to the dynamics of classical subtropical stratocumulus clouds. Unlike subtropical stratocumulus clouds, the WNAO low clouds are spatially uncorrelated with lower tropospheric stability or the anticyclone strength. Instead, CAO index and surface fluxes are the variables that positively correlate with cloud area fraction (west of the cyclonic region), with a circulation that promotes dryness and cooling in the boundary layer. In addition, surface fluxes have important implications for the boundary layer turbulence, aerosol activation, and entrainment of dry air from the free troposphere. Surface fluxes can reconcile the extremely dry boundary layer during the trough pattern with the synoptic peak in low-cloud coverage depicted in Figures 5–7 through turbulent flux enhancement. In addition, Chen et al. (2022) noted that mesoscale simulations of postfrontal cloud fields for the ACTIVATE case of 1 March 2020 were highly sensitive to the SST gradient, which is likely attributed to the role of latent heat fluxes in controlling the boundary layer deepening associated with entrainment. Tornow et al. (2022) computed entrainment rates using in situ and GOES-16 retrievals for the same 1 March 2020 case and found the entrainment rates being an order of magnitude greater than those observed in subtropical stratocumulus clouds regimes. This strong entrainment is expected to modulate the boundary layer deepening, as previously discussed, and can even dominate the CCN budget through the rapid incorporation of aerosols from the overlying free troposphere (Tornow et al., 2022). A more systematic analysis of entrainment rate in postfrontal clouds over WNAO is left for future work.

Our study also provides an alternative characterization of CAOs. Typically, identification of CAOs is determined from a threshold in CAO index (Kolstad et al., 2009), which is in turn applied to generate a composite of atmospheric fields. However, the description of CAO spatiotemporal evolution is scarce in the literature because the CAO identification generally ignores the spatial extent of individual events and the conditions that precede and follow the events (e.g., Fletcher et al., 2016). In our study, the SOM-based clustering allows for the identification of patterns with CAO index >0 , with a peak for the trough, and the coastal detachment during the ridge–trough. Moreover, we suggest that refinements in the CAO categorization can be achieved by directly using SOM 3 (Figure S1 in Supporting Information S1), which is the SOM that characterizes the broadest area with positive CAO index as well as its largest values (up to 9 K).

Synoptic variability also gives rise to enhancements in MODIS cloud droplet number concentrations for the trough and trough–ridge clusters. The prevailing winds for these circulation patterns indicate that likely aerosol sources are located north of the region of study, potentially coming from regions as far north as Canada. However, a puzzling result, also observed at seasonal scale (Dadashazar et al., 2021; Painemal, Corral, et al., 2021; Painemal, Spangenberg, et al., 2021), is the evident lack of synoptic covariability between N_d and AOD. Dadashazar et al. (2021) showed covariations between N_d and AOD in a composite analysis based on samples with N_d that depart by one standard deviation from their seasonal mean. However, they also found that single aerosol species from MERRA-2 yield temporal coefficient of determination (r^2) of equal to less than 0.17. In contrast, ACTIVATE in situ data show a clear spatial covariation between accumulation-mode N_a , CCN, and N_d . The absence of synoptic covariation between MERRA-2 aerosols and MODIS N_d is, thus, attributed to the lack of information of boundary layer variability provided by AOD, large AOD mainly controlled by large particles but with small concentration (particularly for sea salt), as well as issues with the aerosol representation in the model. Another key aspect is the role of turbulent fluxes in aerosol activation through control of supersaturation. For example, CCN concentration below the 1,000 m level for 1 March ranges, on average, between 568 and 1,072 cm^{-3} for supersaturations between 0.15%–0.20% and 0.50%–0.55%, respectively. Our results suggest that both aerosol availability and updraft strength are modulated by the synoptic forcing. Indeed, analysis of ACTIVATE seasonal measurements does indicate the seasonal differences in

N_d can be to a large extent reconciled by changes in updraft speeds between winter and summer (Kirschler et al., 2022).

In this study, we opted for an approach that enabled us to generalize the results based on the zonal progression of the geopotential height at 600 hPa. Refinements in the postprocessing classification can include additional transitions to better describe the trough and ridge evolution. Alternatively, the initial SOMs can be directly applied to the identification of specific synoptic fields. More specifically, for focus on investigating events with a fully developed 600-hPa ridge and surface anticyclone that dominate the entire oceanic domain, it would be reasonable to directly use SOM 13 (Figure 2 and Figure S2 in Supporting Information S1). Another point to consider is that because the SOM algorithm is applied to normalized fields, the detection of extreme events is not necessarily associated with a specific cluster. However, it is apparent from Figures 2 and 3 that the SOM methodology applied here only describes the general evolution of low and high pressures and their eastward evolution. Nevertheless, the extent, magnitude, and track of the pressure systems are not fully represented in our analysis. Davis et al. (1993) document eight distinct storm types over the broad WNAO domain, based on the evolution and location of the cyclonic cores, whereas Reitan (1974) observed four main climatological cyclone tracks. As suggested by these studies, resolving specific spatial features and the diversity of cyclonic activity and evolution will require additional input parameters (e.g., sea-level pressure and wind fields) for the SOM analysis. Lastly, other specific aspects of MBL clouds in midlatitudes such as mesoscale cellular transition, rain and drizzle analysis, and implications for the CCN budget are left for future work. As the ACTIVATE field deployment ended in June 2022, a more comprehensive statistical characterization of different meteorological regimes with in situ observations will be possible in the near future.

6. Summary

Twelve years of MERRA-2 reanalysis geopotential height fields are ingested in a SOM algorithm for generating unsupervised winter synoptic patterns of variability. The well-defined transitions of troughs and ridges allow for an additional regrouping with the main criterion based on the spatial extent of the anomalies and the location of the zero-anomaly axis. This postprocessing reduces the number of synoptic groups to five: ridge, trough–ridge, trough, and ridge–trough, and a fifth pattern governed by meteorological fields that minimally depart from the seasonal climatological mean. Coherent changes in sea-level pressure, MBL winds, and large-scale vertical wind go hand in hand with the geopotential height based synoptic regimes: (a) the ridge regime is associated with well-developed anticyclonic circulation; (b) trough–ridge gives rise to a low-pressure system over the ocean, ascents, and northerly winds over the coastal area; (c) trough is associated with the eastward displacement of the cyclone, coastal subsidence, and northerly winds; and lastly (d) ridge–trough features the development of a surface anticyclone and weak winds along the coast. Changes attributed to each regime are summarized in Figure 13. For simplicity, we focus on a coastal band that extended 4° offshore between 33°N and 40°N. The occurrence of marine low clouds is mainly associated with the trough regime, followed by the trough–ridge (Figure 13a), with both patterns featuring synoptic maxima in cloud top height with statistically significant median values that exceed 2 km (Figure 13b). This boundary layer deepening is also consistent with an increase in low-cloud LWP for the trough–ridge and trough regimes; nevertheless, the interregime variability is significant (Figure 13c). In terms of cloud microphysics, a synoptic peak in N_d is mainly observed for the trough regime over the coastal region (Figure 13e), associated with a maximum in surface heat fluxes that exceeds 500 W m⁻² (Figure 13d), and surpasses by more than 400 W m⁻² the values over the open ocean. Interestingly, changes in AOD are statistically insignificant (Figure 13f).

In situ aircraft observations collected during five consecutive days as part of ACTIVATE in winter 2020 validate, in part, the climatological characterization, confirming the occurrence of high N_d for the days identified as trough. In addition, zonal changes in in situ N_d are consistent with those for aerosol and CCN concentrations. Strong surface fluxes in trough–ridge and trough configurations and their relationship with cloud coverage and N_d imply that boundary-layer dynamics, specifically updraft speeds, are required to explaining synoptic changes in N_d , with potential implications for entrainment of free tropospheric air and the CCN budget.

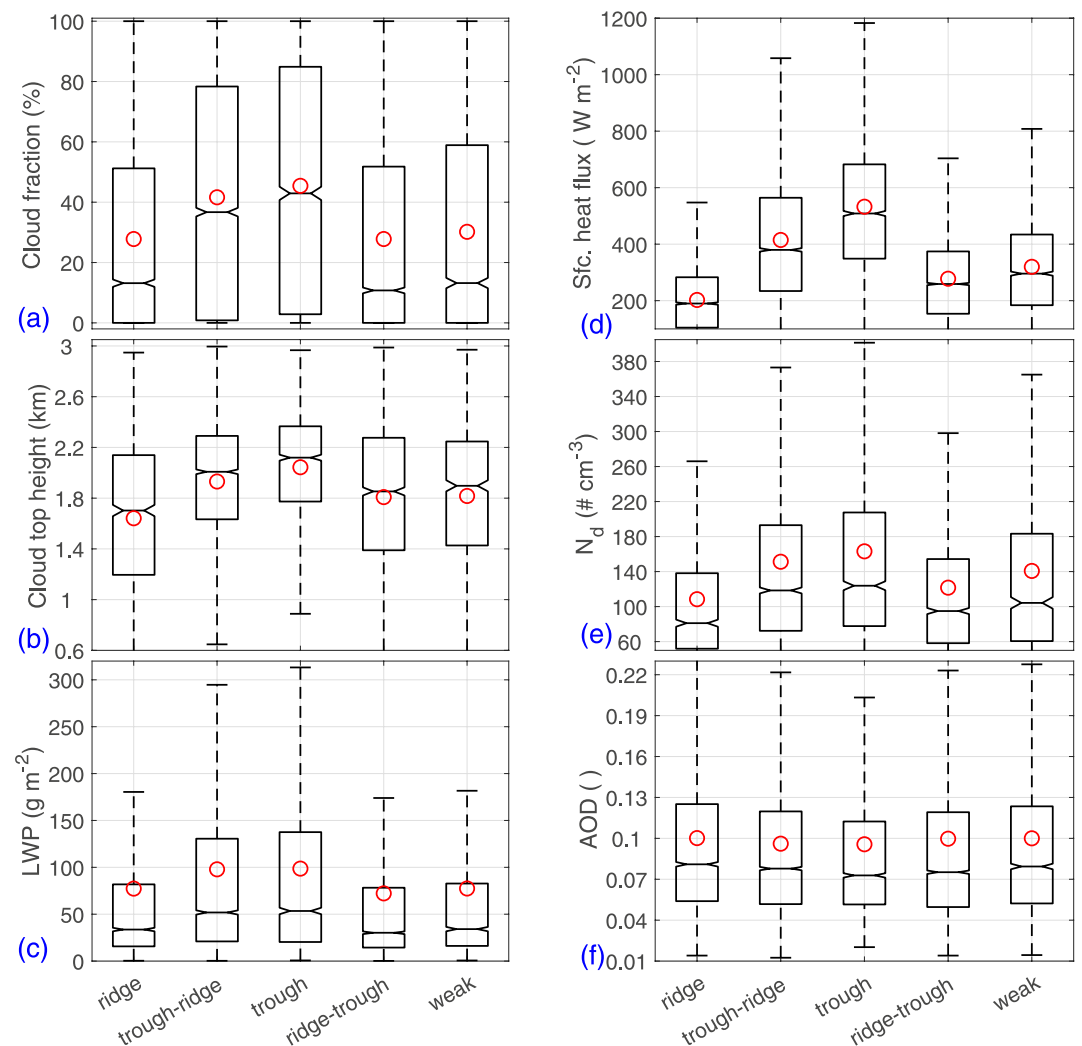


Figure 13. Cloud, aerosol, and thermodynamical properties over a coastal band that extends 4° offshore, between 33°N to 40°N. Horizontal black lines within each box represent the median values, and the edges indicate the lower and upper quartile (25% and 75%). Notches represent the 95% confidence interval of the median. Error bars denote upper and lower 0.7% of a Gaussian distribution. Low error bars are truncated if they reach magnitudes equal or less than 0.0. Red circles are the mean values.

Data Availability Statement

The Aerosol Cloud Meteorology Interactions over the Western Atlantic Experiment data used in this study can be downloaded from the experiment’s repository at <https://doi.org/www-air.larc.nasa.gov/missions/activate/index.html>; <https://doi.org/10.5067/SUBORBITAL/ACTIVATE/DATA001> (ACTIVATE, 2021).

References

ACTIVATE. (2021). *ACTIVATE campaign preliminary repository [collection]*. NASA/Langley Research Center. <https://doi.org/10.5067/SUBORBITAL/ACTIVATE/DATA001>

Berkovic, S. (2017). Winter wind regimes over Israel using self-organizing maps. *Journal of Applied Meteorology and Climatology*, 56(10), 2671–2691. <https://doi.org/10.1175/jamc-d-16-0381.1>

Chang, E. K. M., Lee, S., & Swanson, K. L. (2002). Storm track dynamics. *Journal of Climate*, 15(16), 2163–2183. [https://doi.org/10.1175/1520-0442\(2002\)015<02163:STD>2.0.CO;2](https://doi.org/10.1175/1520-0442(2002)015<02163:STD>2.0.CO;2)

Chang, L.-C., Chang, F.-J., Yang, S.-N., Tsai, F.-H., Chang, T.-H., & Herricks, E. E. (2020). Self-organizing maps of typhoon tracks allow for flood forecasts up to two days in advance. *Nature Communications*, 11(1), 1983. <https://doi.org/10.1038/s41467-020-15734-7>

Chen, J., Wang, H., Li, X., Painemal, D., Sorooshian, A., Thornhill, K. L., et al. (2022). Impact of meteorological factors on the mesoscale morphology of cloud streets during a cold-air outbreak over the western North Atlantic. *Journal of the Atmospheric Sciences*, 79(11), 2863–2879. <https://doi.org/10.1175/jas-d-22-0034.1>

Acknowledgments

The work was funded by NASA Grant 80NSSC19K0442 in support of ACTIVATE, a NASA Earth Venture Suborbital-3 (EVS-3) investigation funded by NASA’s Earth Science Division and managed through the Earth System Science Pathfinder Program Office. CV and SK were funded by the Deutsche Forschungsgemeinschaft (DFG, German Science Foundation) within TRR 301 Project-ID 428312742 and the SPP 1294 HALO under contract VO 1504/7-1. The Pacific Northwest National Laboratory (PNNL) is operated for DOE by the Battelle Memorial Institute under contract DE-AC05-76RLO1830.

- Chin, M., Diehl, T., Ginoux, P., & Malm, W. (2007). Intercontinental transport of pollution and dust aerosols: Implications for regional air quality. *Atmospheric Chemistry and Physics*, 7(21), 5501–5517. <https://doi.org/10.5194/acp-7-5501-2007>
- Dadashazar, H., Painemal, D., Alipanah, M., Brunke, M., Chellappan, S., Corral, A. F., et al. (2021). Cloud drop number concentrations over the western North Atlantic Ocean: Seasonal cycle, aerosol interrelationships, and other influential factors. *Atmospheric Chemistry and Physics*, 21(13), 10499–10526. <https://doi.org/10.5194/acp-21-10499-2021>
- Davis, R. E., Demme, G., & Dolan, R. (1993). Synoptic climatology of Atlantic coast North-Easters. *International Journal of Climatology*, 13(2), 171–189. <https://doi.org/10.1002/joc.3370130204>
- Field, P. R., & Wood, R. (2007). Precipitation and cloud structure in midlatitude cyclones. *Journal of Climate*, 20(2), 233–254. <https://doi.org/10.1175/jcli3998.1>
- Fletcher, J. K., Mason, S., & Jakob, C. (2016). A climatology of clouds in marine cold air outbreaks in both hemispheres. *Journal of Climate*, 29(18), 6677–6692. <https://doi.org/10.1175/jcli-d-15-0783.1>
- Gelaro, R., McCarty, W., Suárez, M. J., Todling, R., Molod, A., Takacs, L., et al. (2017). The Modern-Era Retrospective Analysis for Research and Applications, Version 2 (MERRA-2). *Journal of Climate*, 30(14), 5419–5454. <https://doi.org/10.1175/jcli-d-16-0758.1>
- Gibson, P. B., Perkins-Kirkpatrick, S. E., Uotila, P., Pepler, A. S., & Alexander, L. V. (2017). On the use of self-organizing maps for studying climate extremes. *Journal of Geophysical Research: Atmospheres*, 122, 3891–3903. <https://doi.org/10.1002/2016JD026256>
- Grossman, R. L., & Betts, A. K. (1990). Air–sea interaction during an extreme cold air outbreak from the eastern coast of the United States. *Monthly Weather Review*, 118(2), 324–342. [https://doi.org/10.1175/1520-0493\(1990\)118<0324:AIDAEC>2.0.CO;2](https://doi.org/10.1175/1520-0493(1990)118<0324:AIDAEC>2.0.CO;2)
- Hartmann, D. L., Ockert-Bell, M. E., & Michelsen, M. L. (1992). The effect of cloud type on Earth's energy balance: Global analysis. *Journal of Climate*, 5(11), 1281–1304. [https://doi.org/10.1175/1520-0442\(1992\)005<1281:TEOCTO>2.0.CO;2](https://doi.org/10.1175/1520-0442(1992)005<1281:TEOCTO>2.0.CO;2)
- Hewitson, B. D., & Crane, R. G. (2002). Self-organizing maps: Applications to synoptic climatology. *Climate Research*, 22, 13–26. <https://doi.org/10.3354/cr022013>
- Holt, T. R., & Raman, S. (1990). Marine boundary layer structure and circulation in the region of offshore redevelopment of a cyclone during GALE. *Monthly Weather Review*, 118(2), 392–410. [https://doi.org/10.1175/1520-0493\(1990\)118<0392:MBLSAC>2.0.CO;2](https://doi.org/10.1175/1520-0493(1990)118<0392:MBLSAC>2.0.CO;2)
- Houze, R. A., Jr. (2014). *Cloud dynamics* (2nd ed.), *International geophysics series* (Vol. 104, 432 pp.). Academic Press.
- Kirschler, S., Voigt, C., Anderson, B., Braga, R. C., Chen, G., Corral, A. F., et al. (2022). Seasonal updraft speeds change cloud droplet number concentrations in low level clouds over the western North Atlantic. *Atmospheric Chemistry and Physics*, 22(12), 8299–8319. <https://doi.org/10.5194/acp-22-8299-2022>
- Knop, I., Bansmer, S. E., Hahn, V., & Voigt, C. (2021). Comparison of different droplet measurement techniques in the Braunschweig icing wind tunnel. *Atmospheric Measurement Techniques*, 14(2), 1761–1781. <https://doi.org/10.5194/amt-14-1761-2021>
- Kohonen, T. (2014). *MATLAB implementations and applications of the self-organizing map*. Unigrafia Oy.
- Kohonen, T., Oja, E., Simula, O., Visa, A., & Kangas, J. (1996). Engineering applications of the self-organizing map. *Proceedings of the IEEE*, 84(10), 1358–1384. <https://doi.org/10.1109/5.537105>
- Kolstad, E. W., Bracegirdle, T. J., & Seierstad, I. A. (2009). Marine cold-air outbreaks in the North Atlantic: Temporal distribution and associations with large-scale atmospheric circulation. *Climate Dynamics*, 33(2–3), 187–197. <https://doi.org/10.1007/s00382-008-0431-5>
- Li, X., Wang, H., Chen, J., Endo, S., George, G., Cairns, B., et al. (2022). Large-eddy simulations of marine boundary layer clouds associated with cold-air outbreaks during the ACTIVATE campaign. Part I: Case setup and sensitivities to large-scale forcings. *Journal of the Atmospheric Sciences*, 79(1), 73–100. <https://doi.org/10.1175/jas-d-21-0123.1>
- Mechem, D. B., Wittman, C. S., Miller, M. A., Yuter, S. E., & de Szoeke, S. P. (2018). Joint synoptic and cloud variability over the Northeast Atlantic near the Azores. *Journal of Applied Meteorology and Climatology*, 57(6), 1273–1290. <https://doi.org/10.1175/jamc-d-17-0211.1>
- Minnis, P., Sun-Mack, S., Chen, Y., Chang, F.-L., Yost, C. R., Smith, W. L., et al. (2021). CERES MODIS cloud product retrievals for Edition 4—Part I: Algorithm changes. *IEEE Transactions on Geoscience and Remote Sensing*, 59(4), 2744–2780. <https://doi.org/10.1109/TGRS.2020.3008866>
- Moore, R. H., Wiggins, E. B., Ahern, A. T., Zimmerman, S., Montgomery, L., Campuzano Jost, P., et al. (2021). Sizing response of the ultra-high sensitivity aerosol spectrometer (UHSAS) and laser aerosol spectrometer (LAS) to changes in submicron aerosol composition and refractive index. *Atmospheric Measurement Techniques*, 14(6), 4517–4542. <https://doi.org/10.5194/amt-14-4517-2021>
- Naud, C. M., Booth, J. F., & Del Genio, A. D. (2014). Evaluation of ERA-interim and MERRA cloudiness in the Southern Ocean. *Journal of Climate*, 27(5), 2109–2124. <https://doi.org/10.1175/JCLI-D-13-00432.1>
- Naud, C. M., Booth, J. F., Jeyaratnam, J., Donner, L. J., Seman, C. J., Zhao, M., et al. (2019). Extratropical cyclone clouds in the GFDL climate model: Diagnosing biases and the associated causes. *Journal of Climate*, 32(20), 6685–6701. <https://doi.org/10.1175/JCLI-D-19-0421.1>
- Nishiyama, K., Endo, S., Jinno, K., Uvo, C. B., Olsson, J., & Berndtsson, R. (2007). Identification of typical synoptic patterns causing heavy rainfall in the rainy season in Japan by a self-organizing map. *Atmospheric Research*, 83(2–4), 185–200. <https://doi.org/10.1016/j.atmosres.2005.10.015>
- Painemal, D. (2018). Global estimates of changes in shortwave low-cloud albedo and fluxes due to variations in cloud droplet number concentration derived from CERES-MODIS satellite sensors. *Geophysical Research Letters*, 45, 9288–9296. <https://doi.org/10.1029/2018GL078880>
- Painemal, D., Corral, A. F., Sorooshian, A., Brunke, M. A., Chellappan, S., Gorooh, V. A., et al. (2021). An overview of atmospheric features over the western North Atlantic Ocean and North American East Coast: 2. Circulation, boundary layer, and clouds. *Journal of Geophysical Research: Atmospheres*, 126, e2020JD033423. <https://doi.org/10.1029/2020JD033423>
- Painemal, D., Spangenberg, D., Smith, W. L., Jr., Minnis, P., Cairns, B., Moore, R. H., et al. (2021). Evaluation of satellite retrievals of liquid clouds from the GOES-13 imager and MODIS over the midlatitude North Atlantic during the NAAMES campaign. *Atmospheric Measurement Techniques*, 14(10), 6633–6646. <https://doi.org/10.5194/amt-14-6633-2021>
- Papritz, L. (2017). Synoptic environments and characteristics of cold air outbreaks in the Irminger Sea. *International Journal of Climatology*, 37, 193–207. <https://doi.org/10.1002/joc.4991>
- Reitan, C. H. (1974). Frequencies of cyclones and cyclogenesis for North America, 1951–1970. *Monthly Weather Review*, 102(12), 861–868. [https://doi.org/10.1175/1520-0493\(1974\)102<0861:FOCACF>2.0.CO;2](https://doi.org/10.1175/1520-0493(1974)102<0861:FOCACF>2.0.CO;2)
- Rossow, W. B., & Schiffer, R. A. (1999). Advances in understanding clouds from ISCCP. *Bulletin of the American Meteorological Society*, 80(11), 2261–2288. [https://doi.org/10.1175/1520-0477\(1999\)080<2261:AIUCFI>2.0.CO;2](https://doi.org/10.1175/1520-0477(1999)080<2261:AIUCFI>2.0.CO;2)
- Seethala, C., Zuidema, P., Edson, J., Brunke, M., Chen, G., Li, X.-Y., et al. (2021). On assessing ERA5 and MERRA2 representations of cold-air outbreaks across the Gulf Stream. *Geophysical Research Letters*, 48, e2021GL094364. <https://doi.org/10.1029/2021GL094364>
- Shaman, J., Samelson, R. M., & Skillingstad, E. (2010). Air–sea fluxes over the Gulf Stream region: Atmospheric controls and trends. *Journal of Climate*, 23(10), 2651–2670. <https://doi.org/10.1175/2010Jcli3269.1>

- Sorooshian, A., Anderson, B., Bauer, S. E., Braun, R. A., Cairns, B., Crosbie, E., et al. (2019). Aerosol–cloud–meteorology interaction airborne field investigations: Using lessons learned from the U.S. West Coast in the design of activate off the U.S. East Coast. *Bulletin of the American Meteorological Society*, *100*(8), 1511–1528. <https://doi.org/10.1175/bams-d-18-0100.1>
- Sorooshian, A., Atkinson, J., Ferrare, R., Hair, J., & Ziemba, L. (2021). Taking flight to study clouds and climate. *Eos*, *102*. <https://doi.org/10.1029/2021EO158570>
- Su, W., Loeb, N. G., Xu, K.-M., Schuster, G. L., & Eitzen, Z. A. (2010). An estimate of aerosol indirect effect from satellite measurements with concurrent meteorological analysis. *Journal of Geophysical Research*, *115*, D18219. <https://doi.org/10.1029/2010JD013948>
- Tornow, F., Ackerman, A. S., Fridlind, A. M., Cairns, B., Crosbie, E. C., Kirschler, S., et al. (2022). Dilution of boundary layer cloud condensation nucleus concentrations by free tropospheric entrainment during marine cold air outbreaks. *Geophysical Research Letters*, *49*, e2022GL098444. <https://doi.org/10.1029/2022GL098444>
- Vesanto, J., & Alhoniemi, E. (2000). Clustering of the self-organizing map. *IEEE Transactions on Neural Networks and Learning Systems*, *11*(3), 586–600. <https://doi.org/10.1109/72.846731>
- Vesanto, J., Himberg, J., Alhoniemi, E., & Parhankangas, J. (1999). Self-organizing map in Matlab: The SOM toolbox. In *Proceedings of the Matlab DSP Conference* (pp. 16–17).
- Welty, J., & Zeng, X. (2021). Characteristics and causes of extreme snowmelt over the Conterminous United States. *Bulletin of the American Meteorological Society*, *102*(8), E1526–E1542. <https://doi.org/10.1175/bams-d-20-0182.1>
- Wentz, F. J., & Meissner, T. F. (2007). Algorithm Theoretical Basis Document (ATBD): AMSR-E ocean algorithms. RSS Tech. Rep. 051707, 6. Retrieved from http://images.remss.com/papers/amstr/AMSR_Ocean_Algorithm_Version_2_Supplement_1.pdf
- Wood, R. (2012). Stratocumulus clouds. *Monthly Weather Review*, *140*(8), 2373–2423. <https://doi.org/10.1175/mwr-d-11-00121.1>
- Yu, L., & Weller, R. A. (2007). Objectively analyzed air–sea heat fluxes for the global ice-free oceans (1981–2005). *Bulletin of the American Meteorological Society*, *88*(4), 527–540. <https://doi.org/10.1175/bams-88-4-527>
- Zelinka, M. D., Myers, T. A., McCoy, D. T., Po-Chedley, S., Caldwell, P. M., Ceppi, P., et al. (2020). Causes of higher climate sensitivity in CMIP6 models. *Geophysical Research Letters*, *47*, e2019GL085782. <https://doi.org/10.1029/2019GL085782>